Editor's Pick

On the thermodynamics of plasticity during quasi-isentropic compression of metallic glass

View Online   Export Citation   CrossMark

Kaiguo Chen,[1,2,a] (ID) Bo Chen,[1,2] Yinan Cui,[3] Yuying Yu[4] Jidong Yu,[4] Huayun Geng,[4] (ID) Dongdong Kang,[1,2] (ID)
Jianhua Wu,[1,2] Yao Shen,[5,a] (ID) and Jiayu Dai[1,2,a] (ID)

AFFILIATIONS

[1] College of Science, National University of Defense Technology, Changsha 410073, People's Republic of China
[2] Hunan Key Laboratory of Extreme Matter and Applications, National University of Defense Technology, Changsha 410073, People's Republic of China
[3] Applied Mechanics Laboratory, Department of Engineering Mechanics, School of Aerospace, Tsinghua University, Beijing 100084, People's Republic of China
[4] Institute of Fluid Physics, China Academy of Engineering Physics, Mianyang, People's Republic of China
[5] Department of Material Science and Technology, Shanghai Jiao Tong University, Shanghai, People's Republic of China

[a] Authors to whom correspondence should be addressed: chenkaiguo@nudt.edu.cn; yaoshen@sjtu.edu.cn; and jydai@nudt.edu.cn

ABSTRACT

Entropy production in quasi-isentropic compression (QIC) is critically important for understanding the properties of materials under extreme conditions. However, the origin and accurate quantification of entropy in this situation remain long-standing challenges. In this work, a framework is established for the quantification of entropy production and partition, and their relation to microstructural change in QIC. $Cu_{50}Zr_{50}$ is taken as a model material, and its compression is simulated by molecular dynamics. On the basis of atomistic simulation-informed physical properties and free energy, the thermodynamic path is recovered, and the entropy production and its relation to microstructural change are successfully quantified by the proposed framework. Contrary to intuition, entropy production during QIC of metallic glasses is relatively insensitive to the strain rate $\dot{\gamma}$ when $\dot{\gamma}$ ranges from 7.5×10^8 to $2 \times 10^9/s$, which are values reachable in QIC experiments, with a magnitude of the order of $10^{-2} k_B$/atom per GPa. However, when $\dot{\gamma}$ is extremely high ($>2 \times 10^9/s$), a notable increase in entropy production rate with $\dot{\gamma}$ is observed. The Taylor–Quinney factor is found to vary with strain but not with strain rate in the simulated regime. It is demonstrated that entropy production is dominated by the configurational part, compared with the vibrational part. In the rate-insensitive regime, the increase in configurational entropy exhibits a linear relation to the Shannon-entropic quantification of microstructural change, and a stretched exponential relation to the Taylor–Quinney factor. The quantification of entropy is expected to provide thermodynamic insights into the fundamental relation between microstructure evolution and plastic dissipation.

I. INTRODUCTION

Dynamic compression, including adiabatic shock compression (ASC) and quasi-isentropic compression (QIC), is of significant interest in inertial confinement fusion,[1–6] laboratory astrophysics,[7,8] and other high-pressure environments.[9,10] In general, QIC is a process that lies between ASC and the conceptual nondissipative isentropic compression (ISE), but is closer to ISE in most cases.[11–19] By contrast, ASC produces massive amounts of heat and entropy, easily leading to melting.[12,19] The heating caused by plastic deformation usually echoes the increase in entropy in these types of compression and significantly affects the states of solids along the compression path. On the other hand, the microstructure that is created by plastic deformation and carries plasticity exhibits substantial dissimilarities between QICs with different strain rates and ASC.[20,21] However, despite its importance, there is still only limited understanding of the

relationship between plasticity and entropy production in dynamic compression.

The temperature increase ΔT in QIC can be decomposed into two components: the isentropic temperature increase ΔT_{ise} and the excess temperature increase ΔT_{excess}. The former is caused by a reduction in atomic spacing and is reversible upon decompression,[22,23] and it should be path-insensitive. The latter, which echoes the entropy increase, is irreversible upon decompression and can be path-sensitive (e.g., rate-sensitive).[24,25] It is generally supposed that ΔT_{excess} is produced in solids by thermomechanical conversion from plastic work, which is associated with evolution of strength and microstructure. It is also generally accepted that the yield strength of a given metal may undergo an abrupt increase when the strain rate increases beyond 10^6/s.[26–33] Such an increase in strength can be described by semiphenomenological models such as the Zerilli–Armstrong model,[34] the Preston–Tonks–Wallace model,[35] and the Steinberg–Guinan model.[36,37] Characterization of microstructure evolution in dynamic compression have benefited very much from recent progress in dynamic x-ray diffraction (DXRD) technique and atomistic simulations. Phenomena including the transition from dislocation-dominated to twin-dominated plasticity and variations in dislocation and pattern as the strain rate increases in QIC have been observed both numerically and experimentally.[20,21,38,39] On the other side, a temperature rise can have a significant impact on the properties of solids, including changes in the elastic modulus,[28,40] the initiation of phase transitions under extreme conditions,[27,41,42] and inevitably changes in strength.[26,28,30,43] In addition, ΔT_{excess} under compression might cause an additional thermoelastic volumetric change,[32,44,45] leading to another coupling in solids between the isotropic and deviatoric responses, described by the equation of state and the strength model, respectively. The understanding of temperature increase is crucial to obtaining an understanding of these couplings and predicting the variation of related properties.[18] Unfortunately, it is not feasible to infer ΔT_{excess} from temperature data, owing to both experimental and theoretical challenges.

To estimate ΔT_{excess} and quantify entropy production, one method is to use elastoplastic hydrodynamic simulations with a continuum model (the Taylor–Quinney factor β_{int})[31,32,46–48] or discrete dislocation dynamics,[49] which assumes that solids convert plastic work to heat in a constant ratio.[46] Although the typical range of β_{int} is 0.9–1.0 in elastoplastic hydrodynamic simulations of dynamic compression, β_{int} has been shown to vary with factors such as strain, strain rate, and internal material structure in deformations in the absence of hydrodynamic pressure.[50–54] In particular, Lazicki et al.[27] have recently used DXRD to determine solid carbon phases in QIC and have conjectured that β_{int} for solid carbon may vary between 0.5 and 0.9. A similar technique has also been utilized to assist the development of strength models.[55] Several atomistic simulations have shown that β_{int} for plastic deformations under ambient conditions varies with crystal structure.[56,57] Despite this limited progress, there is still a lack of experimental knowledge of β_{int} at extremely high strain rates ($>10^5$/s), hindering understanding QIC in terms of entropy production.

From the perspective of statistical physics, entropy production is related to heat flow between the atomic vibrational subsystem and the configurational subsystem.[58–64] The entropy increase contains contributions from both of these subsystems. The former is

related to plastic heating, reflecting the portion of plastic work converted into heat, $\beta_{int}W_p$. The latter should be correlated with the pattern of microstructures, which also store a portion of plastic work as what is known as cold energy, $(1 - \beta_{int})W_p$.[57,61,65] The interplay between plastic heating and microstructure evolution is a very unclear dynamic process. In general, the free energy of a system has the form $U - TS$, in which U is internal energy and S is entropy. Plastic heating and cold energy both have contributions from changes in both U and TS. Berdichevsky[66–68] has pointed out that the lack of a plasticity model with satisfactory predictive capability may stem from the fact that our understanding of entropy for microstructures, which should serve as a key thermodynamic parameter, is very limited. Rao et al.[69] and Xiao et al.[70] have implemented the idea mentioned above to develop a two-temperature strength model for glassy systems. However, there is a lack of any direct link between microstructure characterization and thermodynamic entropy.

Our work reported here aims to provide thermodynamic insights into plastic deformation in QIC. For simplicity, a material that is isotropic, namely, metallic glass (MG), is taken as the model. We establish a partition of plastic work into heating and stored energy, quantify entropy production, derive its relationship with plastic work, and establish a partition into vibrational and configurational parts. The remainder of the article is organized as follows. Section II discusses the definition of a quasi-isentrope, on the basis of which simulation methods are developed and quasi-isentropic compression is demonstrated. Section III provides a detailed description of our analytical framework. Calculation of entropy production and its relationship with plasticity in nonequilibrium molecular dynamics (NEMD)-QIC are presented in Sec. IV. Section V presents conclusions.

II. SIMULATION AND DEFINITION OF QUASI-ISENTROPE

A. Metallic glass sample preparation and consideration

A typical MG, $Cu_{50}Zr_{50}$, is chosen as the research model for three reasons. First, the isotropic nature of an MG allows simple mechanical analysis of, for example, strain decomposition. Second, size effects in molecular dynamics simulations of MGs are relatively smaller than in crystalline materials; see, for example, cases 1 and 2 in Ref. 71 and the results provided in the supplementary material. These small size effects in MGs are due to the fact that the mechanical interactions of an MG's structural units decay as $1/r^{~2}$ rather than the $1/r$ decay exhibited by dislocations in crystalline materials.[72] Third, the free energy and entropy during heating have been well studied in Ref. 73, providing a benchmark for our calculations. A small MG sample (S-Sample), containing 4000 atoms (dimensions $4 \times 4 \times 4$ nm^3), is prepared by rapid quenching from 2000 to 0.1 K in 200 ns. Subsequently, the sample is heated for 100 ps to 600 K, followed by relaxation at 600 K for 50 ns, after which it is cooled gradually to the target temperature. The glass transition temperature T_g of the sample is ~620 K, as reported in Ref. 73. The atomic interaction in the MG is described by the embedded atom method (EAM) potential.[74] All simulations are carried out using the Large-scale Atomic/Molecular Massively Parallel Simulator (LAMMPS) package.[75,76] Timesteps are 1 fs for all simulations in this article. In contrast to the conventional usage in mechanics,

positive values denote compressive stress and strain in this work, whereas negative values indicate tensile stress and strain.

B. Quasi-isentropic compression simulations

Nonequilibrium molecular dynamics (NEMD) simulation are is employed to create quasi-isentropic compression of the MG. In particular, as well as ramp compression,[21,24] another two artificial compressions are also simulated and analyzed, as depicted in Fig. 1(a), to exclude other potential dissipative mechanisms and to verify the validity of the proposed framework. The first compression method is uniaxially adiabatically compression (UC-QIC) of the S-Sample with controlled strain rate and no pressure and temperature control (*NVE*). UC-QIC results in a uniaxial strain state ($\varepsilon_n \equiv \varepsilon_{zz} = \Delta\rho/\rho > 0$ and $\varepsilon_t \equiv \varepsilon_{xx} = \varepsilon_{yy} = 0$, where x, y and z are Cartesian coordinates, n represents the compressional direction, and t is orthogonal to n). Periodic conditions are applied to the x, y, and z directions. The computational cost of UC-QIC is relatively low, and therefore the effects of both size and strain rate in uniaxial compression are tested by UC-QIC cases. The results show that both the size effect and the effect of strain rate >10^8/s on yield strength and temperature rise in UC-QIC are negligibly small (see Fig. S7, supplementary material).

The second compression method in this study is based on NEMD simulation of ramp wave propagation (NEMD-QIC) in a long sample (L-Sample), also leading to a uniaxial strain state. NEMD-QIC simulates experimental QIC. The L-Sample, containing 3×10^7 atoms, has dimensions $20 \times 20 \times 1200$ nm^3, obtained by repeating the S-Sample $5 \times 5 \times 300$ times. A flyer, whose particle velocity increases from zero to 1200 m/s in a rise time t_{rise}, moves from the lower end toward the upper end of the L-Sample, generating a ramp wave propagating toward the upper end within the sample along the z direction. Periodic conditions are applied to the x and y directions. NEMD-QIC is characterized by t_{rise}, during which time the pressure and density increase smoothly to a peak, as described in Refs. 21 and 24. t_{rise} is related to the strain rate according to $\dot{\gamma} \propto 1/t_{rise}$. The rise time and propagation distance ($L \propto Ct_{rise}$, where C is the wave velocity) achieved in NEMD-QIC are at least an order of magnitude lower than those in experiments.

The third compression method is "pseudo" isentropic compression (pISE) achieved through isotropic adiabatic compression of the S-Sample without pressure and temperature control ($\varepsilon_n = \varepsilon_t = \frac{1}{3}\Delta\rho/\rho > 0$), with periodic conditions along the x, y, and z directions. Note that NEMD-QIC results in spatial thermodynamic gradients ($\nabla\rho, \nabla T, \nabla P, \ldots$) along the wave propagation direction n. By contrast, these gradients are not present in UC-QIC and pISE.

The three compression methods can lead to several potential candidate dissipative mechanisms,[31,32] with plasticity possibly being dominant. The first mechanism is linked to the uniaxial strain state, which results in an increase in deviatoric strain ($\gamma \equiv \varepsilon_{zz} - \varepsilon_{yy} > 0$) and subsequently yields plastic deformation in solids. The second is based on the familiar concept of artificial bulk viscosity[77] acting in the presence of a pressure gradient. The third is heat conduction due to the presence of a temperature gradient. All of these mechanisms can produce excess temperature and entropy increase. In contrast to NEMD-QIC, for UC-QIC, only plastic deformation is a candidate dissipative mechanism, owing the absence of gradients. Note that pISE provides a nondissipative compression benchmark. The term "pseudo" implies a small deviation from a perfect isentrope. Figures 1(b) and 1(c) demonstrate that the P–ρ–T paths in NEMD-QIC and UC-QIC almost completely overlap with that in pISE in early-stage compression, indicating that the behavior in this regime is consistent with an ideal isentrope. Dissipation may begin to appear in NEMD-QIC and UC-QIC at $\rho/\rho_0 \approx 1.1$, where, as we will show later, yielding occurs, resulting in a significant deviation from pISE as depicted in Fig. 1(b).

We must stress that a comparison of the results for NEMD-QIC and UC-QIC in Fig. 1(b) may lead to an illusion that the pressure
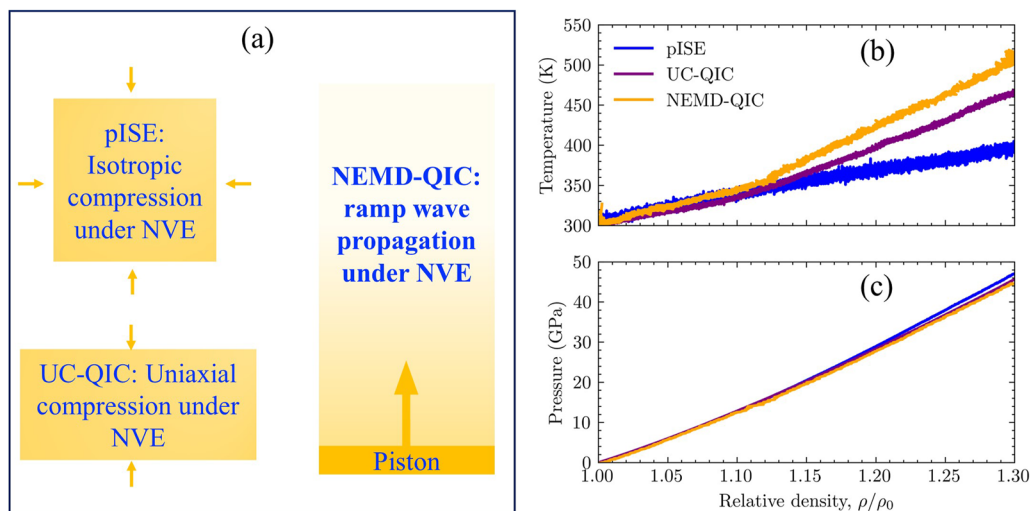

FIG. 1. (a) Illustrations of three different compression simulations: pISE, UC-QIC, and NEMD-QIC. (b) and (c) Thermodynamic paths undergone by Cu$_{50}$Zr$_{50}$ metallic glass subjected to pISE, UC-QIC, and NEMD-QIC at an equivalent strain rate of ~7.5 × 10^8/s.

and temperature gradient contribute to the temperature increase in NEMD-QIC. However, we argue that the temperature increase induced by heat conduction in ramp compression at low pressure is negligibly small. The thermal conductivity κ of our MG sample is calculated by the Green–Kubo method,[78] which relates the ensemble average of the autocorrelation of the heat flux J to κ through $\kappa = \left(V/3k_BT^2\right)\int_0^\infty \langle J(0)J(t)\rangle \mathrm{d}t$. The autocorrelation of J is computed for the small sample under the microcanonical ensemble. The results show an increase in κ from ~0.6 W/mK at 0 GPa to ~1.5 W/mK at 40 GPa (T = 300 K). The heat flow q caused by the temperature gradient is estimated as $q = \kappa \nabla T \approx \kappa T_{\max}/Ct_{\mathrm{rise}}$, where $T_{\max}$ is the maximum temperature increase achieved in a Lagrange element and C is, for example, 5000 m/s. Therefore, the temperature increase caused by heat conduction in a time duration t_{rise} can be estimated: $\Delta T_c \approx \kappa(T_{\max}/Ct_{\mathrm{rise}})(1/\rho C\,C_V)$. Under the assumption that the maximum temperature increase is not too high (e.g., 200 K), $\Delta T_c < 0.1$ K is negligibly small for $t_{\mathrm{rise}} > 10$ ps. Obviously, ΔT_c as a fraction of the total temperature increase is $\Delta T_c/T_{\max} < 0.001$ for $t_{\mathrm{rise}} > 10$ ps and $\Delta T_c/T_{\max} < 0.000\,01$ for $t_{\mathrm{rise}} > 1$ ns. If the density is not high enough to lead to an order-of-magnitude increase in κ,[79] then heat conduction in ramp compression can be ignored. In this study, the rise times vary from 10 to 400 ps, for which gradients may not be manifested.

C. Discussion of isentrope and quasi-isentrope

Before proceeding any further, we first present a conceptual discussion on the deviation from isentropic behavior. Figure 2 illustrates the increase in temperature with density under compression. It must be emphasized that, unlike plastic deformation with no pressure, a "perfect" reference isentrope can be established in dynamic compression from the initial state, along which there is no irreversible nonaffine deformation or microstructural change, an example being the conditions expected in pISE. This idealized isentropic path is represented by the solid blue line in Fig. 2. In dynamic compression, isentropic compression consumes the least energy. By contrast, in the case of QIC, plastic deformation is inevitable, leading to a waste of energy in dissipation. The quasi-isentrope yielded by experiments is shown by the red solid line in Fig. 2. A state C along the quasi-isentrope can be described by $[T(C),\rho(C),\gamma_a(C)\neq0,\ldots]$, where T is the temperature, ρ is the density, and γ_a measures the inevitable microstructural change. For a given state C, it is possible
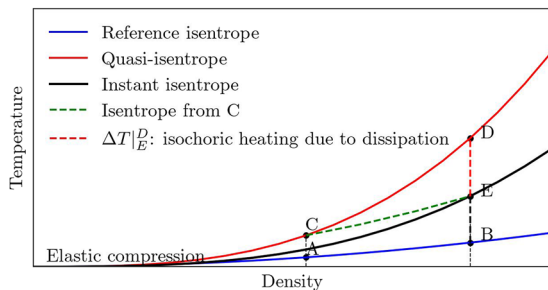

FIG. 2. Illustration of the reference isentrope, instant isentrope, and quasi-isentrope without phase transition. States A and C have the same density, and states B, D, and E have the same density.

to define a corresponding reference isentropic state A with identical density, by $[T(A),\rho(A)=\rho(C),\gamma_a(A)=0,\ldots]$. Before significant dissipation occurs, such as in the case of elastic compression, the temperature at state A, $T(A)$, can be assumed to be equal to the temperature at state C, $T(C)$. Along the perfect isentrope, the temperature is approximated by integrating over a small duration using the expression $\mathrm{d}T_{\mathrm{ise}}|_A^B = -T(A)\gamma_g(A)\mathrm{d}\ln(\rho_A/\rho_B)$, where γ_g is the state-dependent Grüneisen parameter. However, we can only observe state C, with detailed atomic trajectories, in simulations but very limited observables in experiments. Hence, an isentropic path starting from state C is defined as $\mathrm{d}T_{\mathrm{ise}}|_C^E = -T(C)\gamma_g(C)\mathrm{d}\ln(\rho_A/\rho_B)$. To reach state D on the quasi-isentropic path, isochoric heating is required to compensate for the dissipation that occurs during compression from state E. By integrating $\mathrm{d}T|_E^D = \mathrm{d}T|_C^D - \mathrm{d}T_{\mathrm{ise}}|_C^E$, the amount of dissipation can be quantified.

The recovery of the reference isentrope is facilitated by the accumulated dissipation. In hydrodynamic simulations, the determination of the differential form $\mathrm{d}T|_C^D$ for temperature change along QIC can be expressed as[44]

$$\mathrm{d}T|_C^D = -T\gamma_g(\rho,T)\,\mathrm{d}\ln\left(\frac{\rho_0}{\rho}\right) + \frac{T\,\mathrm{d}S}{C_V(\rho,T)}, \qquad (1)$$

where C_V is the isochoric heat capacity. The first term on the right-hand side of Eq. (1) is identical to $\mathrm{d}T_{\mathrm{ise}}|_C^E$. The second term, on the other hand, pertains to the dissipation contribution. It is worth noting that the black line, which results from integrating $\mathrm{d}T_{\mathrm{ise}}|_C^E = -T(C)\gamma_g(C)\mathrm{d}\ln(\rho_A/\rho_B)$, represents an instant isentrope rather than the reference isentrope. The difference between the temperature increase along the instant isentrope and that along the reference isentrope is given by $\Delta T_{\mathrm{err}} = \Delta T|_C^E - \Delta T|_A^B = \int[T(A)\gamma_g(A) - T(C)\gamma_g(C)]\mathrm{d}\ln(\rho_A/\rho_B)$, which may increase as the compression proceeds. In general, $\Delta T|_B^E > \Delta T|_A^C$ is expected, because of the difference between states A and C, raising subtle arguments about the reference isentrope. This difference is negligible when the temperature is as small as <600 K in our simulations.

The reference isentrope should be a fundamental property of a solid material that remains unchanged under varying compression methods, as long as there is no path-dependent phase transition. In our study, we quantify dissipation by rewriting Eq. (1) as

$$\mathrm{d}S = \frac{C_V(\rho,T)\,\mathrm{d}T}{T} + \gamma_g(\rho,T)C_V(\rho,T)\,\mathrm{d}\ln\left(\frac{\rho_0}{\rho}\right), \qquad (2)$$

and the entropy can be directly obtained by integrating this equation along the compressional path. The excess temperature increase appears as $\Delta T_{\mathrm{excess}} = \int T\mathrm{d}S/C_V$. The recovery of the reference isentrope is achieved by $\Delta T_{\mathrm{ise}} = \Delta T - \Delta T_{\mathrm{excess}}$.

III. INTEGRATED ANALYSIS FRAMEWORK

A. Integrating plastic deformation, microstructural change, and thermodynamics

Our framework as illustrated in Fig. 3 aims to mine the data, from the perspective that it is the plasticity that contributes to dissipation and microstructural change. First, the fraction of the plastic work converted into heat, as the Taylor–Quinney factor, is calculated. As discussed in Sec. II C, we already have the plastic heat $Q = \int_{\rho_0}^\rho T\mathrm{d}S = \int_{\rho_0}^\rho C_V\mathrm{d}T_{\mathrm{excess}}$ on hand according to Eqs. (1) and (2).
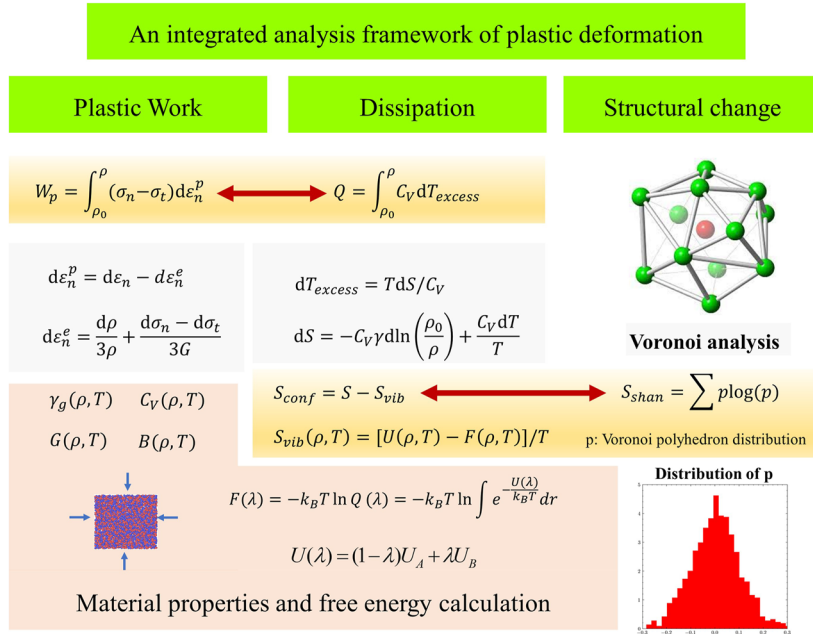
FIG. 3. Illustration of the framework integrating thermodynamics, mechanics, and microstructural analysis.

To quantify plastic work, the Taylor strain condition is utilized to decompose uniaxial strain ε_n into an elastic contribution ε_n^e and a plastic contribution ε_n^p:[31,44]

$$d\varepsilon_n^e = \frac{d\rho}{3\rho} + \frac{d\sigma_n - d\sigma_t}{3G(\rho, T, \gamma_a)}, \quad d\varepsilon_n^p = d\varepsilon_n - d\varepsilon_n^e, \quad (3)$$

in which only the state-dependent shear modulus G is employed. Density, normal stress $\sigma_n = \sigma_{xx}$, and transverse stress $\sigma_t = 0.5(\sigma_{yy} + \sigma_{zz})$ are from molecular dynamics (MD) data. The strain in Eq. (3) is directly computed from MD simulations as $d\varepsilon_n = d\rho/\rho$. Plastic heating is not considered. According to the Lindemann-like rule,[80] the linear thermal expansion caused by additional heat produced by plastic work is negligible as estimated by $0.75 \times 10^{-2}\Delta T/T_g$ (<0.005). Plastic work $dW_p = (\sigma_n - \sigma_t)d\varepsilon_n^p$ and $\beta_{int} = Q/W_p$ then appear as functions of ε_n^p.

Second, we try to establish a connection between dissipation and microstructural change. As well as the part of the plastic work converted into dissipation, another part is stored as internal energy for microstructural change (without TS term): for example, defect energy in crystalline metals. However, the microstructural change also contributes to entropy increase by its disorder. We notice that the entropy S obtained by integrating Eq. (2) along the compressional path can be decomposed into vibrational and configurational components.[59,73] S directly quantifies the dissipation. Following the Boltzmann relation, we have $S = k_B \ln \Omega \sim k_B \ln (\Omega^v \Omega^c) = k_B \ln \Omega^v + k_B \ln \Omega^c = S_{vib} + S_{conf}$, in which Ω^v and Ω^c are the number of vibrational and configurational states, respectively, and S_{vib} and S_{conf} are the vibrational and configurational entropies, respectively. To achieve the decomposition, we further notice that the Helmholtz free energy F containing only

a vibrational contribution can be sampled by the Frenkel–Lad method,[73] the details of which will be discussed in Sec. III B. Thus, $S_{vib} = (U - F)/T$ (where U is internal energy) is obtained. Then, the decomposition of ΔS can be approximated by $\Delta S_{conf} = \Delta S - \Delta S_{vib}$. It should be emphasized that there exists a correlation between ΔS_{conf} and microstructural change. Unfortunately, accurate quantification of this correlation remains challenging.[67,68] Borrowing an idea from statistical physics, here we utilize a local structure analysis method, Voronoi polyhedron analysis,[81] to reveal atomic structural changes. The mathematical quantification of microstructure is thus made via local fivefold symmetry (LFFS)[82] and Shannon entropy[83] so as to link with ΔS_{conf}.

Specifically in the case of QIC, the above framework has the capability to accurately determine the increase in entropy, its quantitative relationship with plastic work, and its correlation with changes in microstructure. Notably, it can uncover the configurational contribution to entropy, thereby enabling a thermodynamic characterization of microstructural change, a long-sought goal in materials science.

B. Thermophysical properties calculation

In the above framework, the shear modulus G, heat capacity C_V, Grüneisen parameter γ_g, free energy, and other thermophysical properties are assumed to be state-dependent. This assumption is also widely utilized in elastoplastic hydrodynamic simulations when rough estimates are made.[18,32] For example, $\rho\gamma_g = $ const is usually used.[84] In our study, state-dependent properties are calculated directly from atomistic simulation of a small sample with only 4000 atoms instead of by employing phenomenological laws. Irreversible plastic deformation may impact the physical properties of an

MG. Six samples are systematically prepared by subjecting the initial S-Sample to different levels of plastic deformation through shearing, followed by an un-shearing to a zero-stress state and subsequent *NPT* relaxation. The boundary conditions are consistent with those utilized in UC-QIC and pISE. As a result of the preparation procedure, residual strain is induced in the samples, which is quantified through atomic shear strain calculations.[85] Taking the undeformed S-Sample as the reference configuration, the average atomic shear strains of these samples are determined by the Open Visualization Tool (OVITO)[86] to be $\gamma_a = [0.0, 0.0284, 0.0366, 0.110, 0.137, 0.166]$, respectively. $\gamma_a = 0$ corresponds to the undeformed sample. Each sample is subsequently compressed and heated to map the P–T subspace from 0 to 50 GPa and from 300 to 1200 K in pressure steps of 5 GPa and temperature steps of 50 K. The mechanical modulus is obtained by linear fitting of the strain–stress curve under small compression and shear deformations. The isochoric heat capacity $C_V = -\partial U/\partial T$ and the Grüneisen parameter $\gamma_g = (V/C_V)dP/dT$ are obtained by fitting U–T and P–T curves, respectively, under isochoric heating ($\delta T = 10$ K) from a given (P, T) state. The Helmholtz free energy F and the vibrational entropy $S_{\text{vib}} = (U - F)/T$ are sampled by the Frenkel–Lad method.[73,87] Then, functions of the form $H(\rho, T, \gamma_a) = h_0[1 + h_1\rho/\rho_0 + h_2(\rho/\rho_0)^2](1 + h_3 T + h_4 T^2)(1 + h_5\gamma_a + h_6\gamma_a^2)$ for all properties are prepared for use. $H(\rho, T, \gamma_a)$ assumes a linear deviation from ambient conditions with small density, temperature, and structural changes. h_i ($i = 0, \ldots, 6$) are fitting parameters and are listed in Table I. The detailed calculation of F is discussed below.

The Frenkel–Lad method samples the Helmholtz free energy containing only the vibrational entropy contribution of the MG.[73] The basis of this method is calculation of the free energy difference between a state of interest and a reference state for which an exact solution exists. In this study, an Einstein crystal in which atoms do not interact with each other via an atomic potential, is chosen as the reference state. The free energy difference between a state of interest and this reference state is calculated by the construction of a reversible path connecting a sequence of equilibrium states between the two thermodynamic states. By the introduction of a coupling parameter λ ranging from 0 to 1, the Hamiltonian of the system can change from the Hamiltonian of the Einstein crystal reference state (EC) to the Hamiltonian of the real system (R):

$$U(\lambda) = (1 - \lambda)U_{\text{EC}} + \lambda U_R, \tag{4}$$

where U is internal energy. For the system in the *NVT* ensemble, the free energy F is a function of λ:

$$F(\lambda) = -k_B T \ln Q(\lambda) = -k_B T \ln \int e^{-U(\lambda)/k_B T} dr. \tag{5}$$

The derivative of the free energy with respect to λ can be obtained as

$$\frac{dF(\lambda)}{d\lambda} = \frac{1}{Q(\lambda)} \int e^{-U(\lambda)/k_B T} \frac{\partial U}{\partial \lambda} dr = \left\langle \frac{\partial U}{\partial \lambda} \right\rangle_\lambda. \tag{6}$$

The free energy difference is obtained by integration of this differential equation:

$$\Delta F = \int_0^1 \left\langle \frac{\partial U}{\partial \lambda} \right\rangle_\lambda d\lambda = \int_0^1 \langle U_R - U_{\text{EC}} \rangle d\lambda. \tag{7}$$

The Hamiltonian of the Einstein crystal reference system has the harmonic form

$$H_{\text{EC}} = \sum_{i=1}^N \left[\frac{p_i^2}{2m} + \frac{1}{2}m\omega^2(r_i - r_i^0)^2 \right]. \tag{8}$$

The free energy of the Einstein crystal can be solved for analytically as

$$F_{\text{EC}}(N, V, T) = 3Nk_B T \ln\left(\frac{\hbar\omega}{k_B T}\right), \tag{9}$$

where ω is the oscillator frequency, and the harmonic potential with spring constant ($m\omega^2$) is usually utilized in simulations to describe the Hamiltonians of a reference Einstein crystal. For the MG of interest here, corrections for re-centering of mass need to be considered:

$$\frac{F_{\text{EC}}(N, V, T)}{k_B T} = \sum_{i=\text{Cu,Zr}} x_i \ln\left(\frac{\beta k \Lambda_i^2}{2\pi}\right)^{3/2} - \frac{1}{N}\ln\left(\frac{\beta k}{2\pi \sum_{i=\text{Cu,Zr}} x_i\mu_i^2}\right)^{3/2}$$
$$- \frac{1}{N}\ln V + 2.5N\ln N - \frac{1}{N}\ln\left(\frac{N}{N_{\text{mol}}}\right), \tag{10}$$

where x_i is the mole fraction, $\mu_i = m_i/\sum_{i=\text{Cu,Zr}} m_i$, $\Lambda_i = \sqrt{\beta h^2/2\pi m_i}$ are the wavelengths of copper ($i = 1$) and zirconium ($i = 2$) atoms, and k

TABLE I. Fitting parameters of thermophysical properties of the model $Cu_{50}Zr_{50}$. The equation is $H(\rho, T, \gamma_a) = h_0[1 + h_1\rho/\rho_0 + h_2(\rho/\rho_0)^2](1 + h_3 T + h_4 T^2)(1 + h_5\gamma_a + h_6\gamma_a^2)$, in which ρ is in units of kg/m³, T is in units of K, and γ_a is dimensionless. C_V is the isochoric heat capacity, γ_g the Grüneisen parameter, B the bulk modulus, G the shear modulus, S_{vib} the vibrational entropy, and F the Helmholtz free energy containing only a vibrational contribution.

	h_0	h_1	h_2	h_3	h_4	h_5	h_6
C_V (J mol⁻¹ K⁻¹)	28.6	0.252	−0.140	$−9.44 \times 10^{-4}$	4.67×10^{-7}	−0.145	0.847
γ_g	1.166	4.266	−3.500	$−7.087 \times 10^{-4}$	2.38×10^{-7}	−1.014	4.623
B (GPa)	300.0	−1.796	1.281	1.029×10^{-4}	$−1.35 \times 10^{-7}$	−0.129	5.77×10^{-2}
G (GPa)	10.4	1.47×10^{-3}	2.045	8.264×10^{-4}	4.84×10^{-7}	−1.63	5.56
S_{vib} (k_B/atom)	3.88	−5.27	0.0017	3.28	6.24×10^{-8}	−0.011	0.168
F (eV/atom)	−0.247	2.398	−1.348	$−2.353 \times 10^{-5}$	8.14×10^{-8}	$−5.18 \times 10^{-3}$	0.0352

is the spring constant. With F_{EC} and ΔF, the Helmholtz free energy of the MG is obtained as $F = F_{EC} + \Delta F$, and also the vibrational entropy $S_{vib} = (U - F)/T$.

Figure 4 shows several results for the calculated thermophysical properties according to Table I. To discuss the rationality of these results, a density-sensitive parameter $H_\rho = (1/H)\partial H/\partial \rho$, temperature-sensitive parameter $H_T = (1/H)\partial H/\partial T$, and deformation-sensitive parameter $H_{\gamma_a} = (1/H)\partial H/\partial \gamma_a$ of the thermophysical properties are defined. At the ambient states with small irreversible deformations, it is clear that all these properties are sensitive to temperature, all except heat capacity are sensitive to density, and only shear modulus is sensitive to irreversible deformation. These expected scenarios are shown in Fig. 4. Figures 4(a) and 4(c) show that shear modulus and vibrational entropy are sensitive to density and temperature. Figure 4(c) also indicates a clear separation of glass and liquid states on the map, and it suggests that the glass transition increases with density as expected. The vibrational entropy is not sensitive to plastic strain, because the sampling method is irrelevant to configuration, as confirmed by its small H_{γ_a} according to Table I. The deformation-insensitive isochoric heat capacity as shown in Fig. 4(d) also supports this scenario. In particular, Fig. 4(b) demonstrates that γ_g decreases with increasing density. This trend can be explained by the fact that t phonons also exist in the MG, despite its lack of long-range order.[88] Additionally, $\rho\gamma_g = $ const is not applicable for an MG over wide density and temperature ranges. This is reasonable, considering that $\rho\gamma_g = $ const is only a phenomenological law inferred from ASC experiments that access limited regions of density and temperature

in ρ–T space. Because γ_g plays a key role in determining the isentropic temperature increase according to Eqs. (1) and (2), our method for obtaining γ_g at high pressure and high temperature may be applicable for interpretation of QIC experiments. For instance, γ_g at high density and pressure can be accurately calculated by first-principles calculation or machine-learning-enabled MD with quantum accuracy.

IV. RESULTS AND DISCUSSION

A. Isentrope and the deviation from isentrope in QIC in terms of temperature

With the help of the framework established above, the quantification of dissipation by excess temperature increase is illustrated in Fig. 5(b), enabling decisive exclusion of alternative dissipative mechanisms apart from plasticity. The analysis shows that the process of pISE results in a minimal ΔT_{excess}, indicating a near-isentropic behavior as designed. By comparing Figs. 5(b) and 5(c) in which the strength is calculated by $Y = \sigma_n - 0.5(\sigma_{yy} + \sigma_{zz})$, ΔT_{excess} within the elastic regime in both NEMD-QIC and UC-QIC is negligible, with NEMD-QIC displaying gradients ∇T and ∇P. As discussed in Sec. II B, heat conduction does not lead to significant ΔT_{excess} as $t_{rise} > 10$ ps, as demonstrated in the elastic regime [Fig. 5(b)]. Also, the contribution of the bulk viscosity to dissipation in QIC is small when the magnitude of ∇P is much lower than that at the shock front. This suggests that the contributions from both heat conduction (as discussed in Sec. II B) and bulk viscosity to dissipation in NEMD-QIC are inherently negligible in the elastic regime. After a
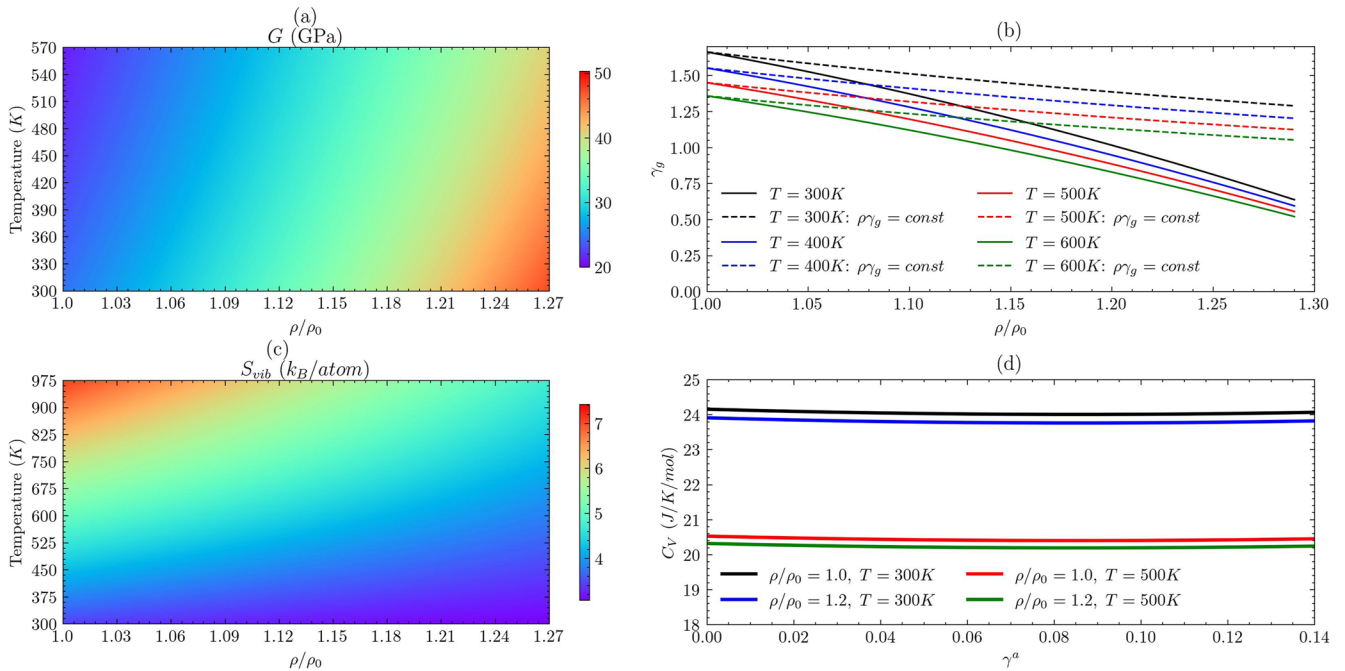

FIG. 4. (a) Shear modulus mapped into pressure and density. (b) Grüneisen parameter vs density at 300, 400, 500, and 600 K. (c) Vibrational entropy mapped into pressure and density. (d) Isochoric heat capacity vs nonaffine atomic strain at different densities and temperatures.
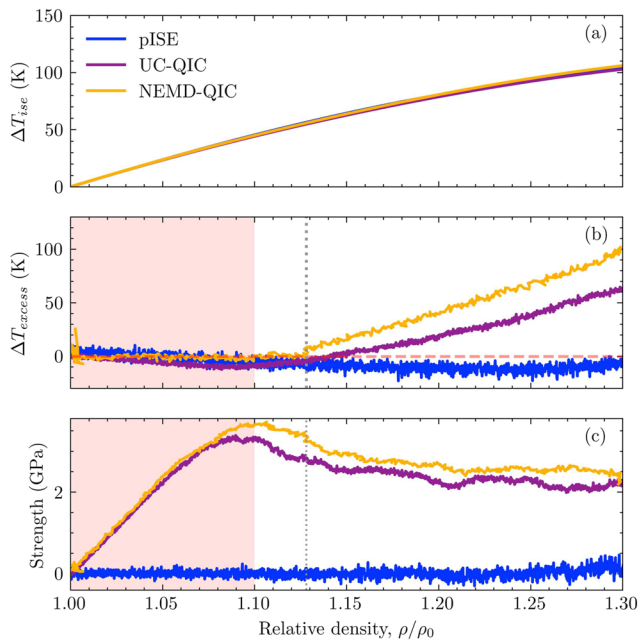
FIG. 5. (a) Isentrope recovered from P–ρ–T path. (b) Excess temperature increase ΔT_{excess} vs density. (c) Strength vs density during pISE, UC-QIC, and NEMD-QIC with an equivalent strain rate of ~$7.5 \times 10^8/\text{s}$. The light red box represents the elastic deformation regime for NEMD-QIC and roughly for UC-QIC. Gray dots indicate where ΔT_{excess} starts to increase.

short period elapsing from yielding [as can be seen by comparing Figs. 5(b) and 5(c)], ΔT_{excess} in NEMD-QIC and UC-QIC begins to increase significantly, while the thermal conductivity and bulk viscosity are not greatly changed by the yielding transition. These findings convincingly demonstrate that plastic deformation dominates dissipation in a MG subjected to QIC, as well as in crystalline solids, despite the distinct microscopic mechanisms involved.[31,32]

By subtracting ΔT_{excess}, the reference isentrope is recovered as a substantial and unchanged property of MG, as illustrated in Fig. 5(a), in which the ΔT_{ise} for NEMD-QIC, UC-QIC, and pISE overlap with each other. In our simulations, we argue that no phase transition occurs in MG. Unlike crystalline solids, MG structures lack long-range order (LRO) and exhibit short-range order changes upon compression, as revealed by Voronoi analysis in terms of local fivefold symmetry (LFFS) increase.[74] The smooth changes in LFFS without disruption of disordered structures in MG suggest the absence of a phase transition. The reference isentrope recovered from all NEMD-QIC and UC-QIC simulations close to the pISE path is thus rational. In addition, it is clear that ΔT_{excess} in NEMD-QIC is higher than that in UC-QIC over the whole plastic deformation, as illustrated in Fig. 5(b). This discrepancy is likely due to the unique deformation protocol employed in UC-QIC, which includes periodic and uniform rescaling of atomic positions followed by a structural relaxation. This rescaling results in an unexpected portion of strain energy being directed toward the microstructural subsystem during the plastic deformation regime. A structural comparison between NEMD-QIC and UC-QIC demonstrates this significant energy flow (see Fig. S11, supplementary material). Thus,

UC-QIC substantially deviates from a real QIC process represented by NEMD-QIC, where plastic deformation and structural change should be taken into account.

B. Rate-insensitive and strain-sensitive Taylor–Quinney factor

An unexpected finding is revealed in regard to the Taylor–Quinney factor β_{int}, which quantitatively measures the relation between plastic work and excess temperature. The results indicate that β_{int} is insensitive to strain rates but sensitive to strain. All β_{int} vs plastic strain curves exhibit the same behavior as the plastic strain increases, converging in the vicinity of one another, as depicted in Fig. 6(b). This outcome contradicts experimental work conducted by Nieto-Fuentes et al.,[53] who found that β_{int} decreases with strain rates that are about six orders of magnitude lower than that in our simulations for a variety of metals. Additionally, an incubation period in which β_{int} remains near zero is observed shortly after yielding. During this period, the plastic work is primarily consumed by microstructural change rather than converted to heat, in parallel with Figs. 5(b) and 5(c). After the incubation period, β_{int} increases monotonically with plastic strain and follows an empirical master curve

$$\beta_{\text{int}}(\varepsilon_p) = \begin{cases} 0, & \varepsilon_p < \varepsilon_p^c, \\ \beta_0 \ln\left(\dfrac{\varepsilon_p}{\varepsilon_p^c}\right), & \varepsilon_p \geq \varepsilon_p^c, \end{cases} \tag{11}$$

where ε_p^c is the ending of the incubation period, and β_0 is a fitting constant. On setting $\beta_0 = 0.45$ and $\varepsilon_p^c = 0.03$, Eq. (11) is found to fit all curves in Fig. 6(b) with satisfactory accuracy. The observed trend strongly suggests that β_{int} is sensitive to structural change in the early stage of plastic deformation. As compression proceeds to the late plastic deformation stage, extrapolation of Eq. (11) suggests that β_{int} reaches a saturation value of unity at $\rho \approx 1.8$. This value is consistent with that typically used in hydrodynamics simulations.[31,32]

C. Rate-insensitive to rate-sensitive transition in entropy production

As an indirect measure of entropy production, quantification of ΔT_{excess} reveals an unexpected rate-insensitive to rate-sensitive transition in entropy production. This is demonstrated in Fig. 6(a), where, for $t_{\text{rise}} > 100$ ps, NEMD-QIC produces ~100 K excess temperature at $\rho/\rho_0 = 1.29$, while the relative isentropic temperature is about 100 K. As t_{rise} decreases to 40 ps, the excess temperature increases to around 120 K. As a comparison, adiabatic shock compression produces ~370 K, which is approached by NEMD-QIC as t_{rise} further decrease. Surprisingly, the presence of rate-insensitive entropy production challenges the conventional understanding obtained from low-strain-rate mechanical tests that plastic heating behavior is rate-sensitive.[51,53] Our simulations suggest that rate-sensitive ΔT in a single-phase solid subjected to high-pressure compression can only be achieved at extremely high strain rates, even though the strength is rate-sensitive over a wide range of strain rates, while a trend of increase in both yield strength Y and W_P at $\rho/\rho_0 = 1.29$ with decreasing t_{rise} is evident.

Phenomenologically, with the quantification of β_{int}, the transition from rate-insensitive to rate-sensitive entropy production can
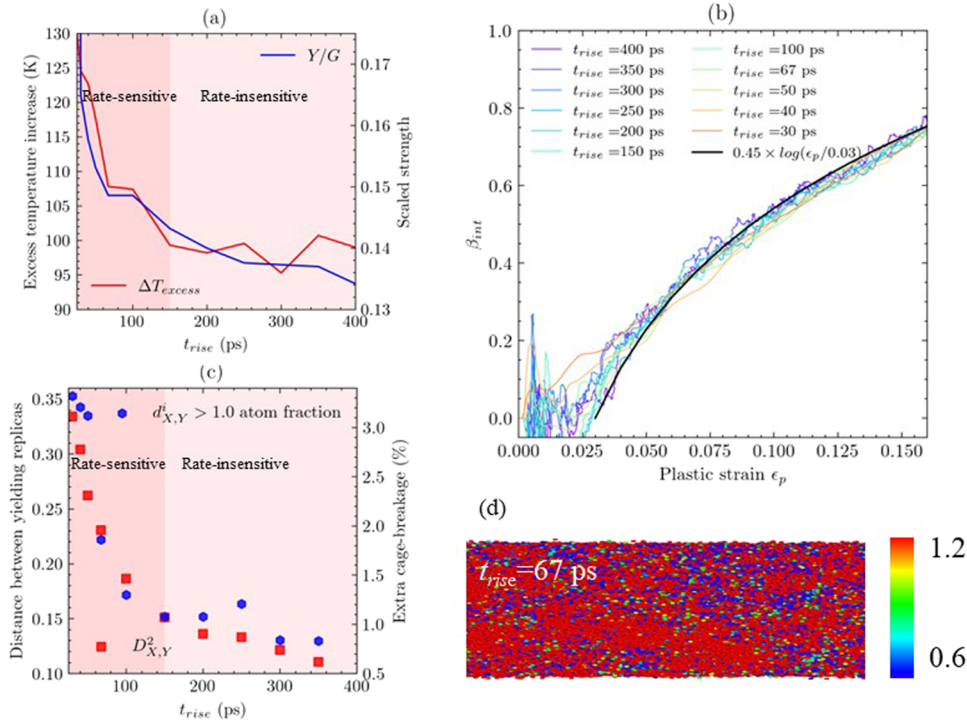
FIG. 6. (a) Excess temperature ΔT_{excess} at $\rho/\rho_0 = 1.29$ and scaled strength vs rise time t_{rise}. A separation between rate-insensitive and rate-sensitive regime is revealed. (b) Taylor–Quiney factor β_{int} vs plastic strain during NEMD-QIC. (c) Replica distance and fraction of extra cage breakage at yielding vs t_{rise}. The separation between rate-insensitive and rate-sensitive regime is the same as in (a). (d) A cross-section colored by $d_{X,Y}^i$ in a yield replica of the case $t_{\text{rise}} = 67$ ps.

be roughly explained by the breakdown of $Y/G^y \approx$ const instead of Y, where Y is the yield strength and G^y is the shear modulus at yielding. This can be argued by a simple scaling. It is noted that ΔT_{excess} should be proportional to $\beta_{\text{int}} \times W_P/\rho$. This scaling is expressed as

$$\Delta T_{\text{excess}} \propto \beta_{\text{int}} \times \frac{W_P}{Y} \times \frac{G^y}{\rho^y} \times \frac{\rho^y}{\rho} \times \frac{Y}{G^y} \propto \beta_{\text{int}} \times \frac{W_P}{Y} \times \frac{G^y}{\rho^y} \times \frac{Y}{G^y}. \quad (12)$$

For all simulated cases, the increase of W_P with strain rate can be attributed to increasing Y ($W_P/Y \approx$ const for all t_{rise}). Also, $G^y/\rho^y \approx$ const for all t_{rise} holds because of the linear dependence of the shear modulus on density at low pressures. Therefore, the following simpler scaling is proposed:

$$\Delta T_{\text{excess}} \propto \beta_{\text{int}} \times \frac{Y}{G^y}. \quad (13)$$

The rate-insensitivity requires that $\beta_{\text{int}} \times Y/G^y$ be independent of t_{rise}. As previously discussed, it is found that there is minimal dependence of β_{int} on t_{rise} in all cases, as illustrated in Fig. 6(b). As a result, the magnitude of entropy production can be attributed to variations in Y/G^y. This relationship is illustrated in Fig. 6(a), where a transition from rate insensitivity to rate sensitivity of Y/G^y can be observed, as well as a corresponding change in entropy production. Thus, Eq. (13) may explain the trend of how entropy production in QIC varies with strain rate.

The observed strain rate dependence of Y/G^y in MGs is in line with previous studies. According to the cooperative shear model (CSM), at low strain rates, a weak rate dependence of Y/G^y in MGs is expected if yielding is viewed as a fold catastrophe.[89] The CSM suggests that MGs contain inherent defects that become activated and contribute to plasticity upon yielding. Measurements of the yielding strength of an MG in a QIC experiment support this hypothesis, since they show a lack of sensitivity around $\dot{\gamma} \sim 10^5/\text{s}$.[90] It has been observed that in many crystalline metals, at higher strain rates, a transition of Y/G^y from rate insensitivity to rate sensitivity occurs at $\dot{\gamma} \sim 10^8/\text{s}$.[31,43,91] This transition may indicate a shift in the mechanism of yielding from activation of existing defects to nucleation of new plasticity carriers such as dislocations.[21,91] On the basis of these findings in crystalline metals, it is hypothesized that a similar transition in the yielding mechanism may occur in MGs.

To further investigate this hypothesis, a concept from statistical physics known as a replica is employed. Specifically, the distance from the atomistic replica for each $t_{\text{rise}}(X)$ to that for $t_{\text{rise}} = 400$ ps (Y only appears as a subscript when representing a replica) is defined as $D_{X,Y}^2 = (1/N)\sum_i d_{X,Y}^i = (1/N)\sum_i (x_X^i - x_Y^i)^2 + (y_X^i - y_Y^i)^2$, where x and y are atom coordinates, and $d_{X,Y}^i$ is the spatial distance between the same atom in different replicas. In an MG, each atom is trapped in a cage formed by its neighboring atoms. On deformation, certain cages may break, serving as plasticity carriers. $d_{X,Y}^i = 1.0$ Å is adopted as a criterion below which the behavior of the cage

centered on atom i is as the same as that at yielding of t_{rise} = 400 ps compression, and above which its behavior deviates from that at yielding of t_{rise} = 400 ps compression. Similarly, $d^i_{X,Y} < 1.0$ Å should be expected if the cages centered on atom i both break or both survive at these two rates. It is supposed that our MG is prepared with born defects. The cages regarded as the born defect may break at yielding for all rates, and thus their center atom will have $d^i_{X,Y} < 1.0$ Å. In the scenario of the CSM, such cage breakages associated with born defects may cooperate, leading to an activation volume of ~100 atoms. Atoms with $d^i_{X,Y} > 1.0$ Å can then be regarded as an extra broken cage by comparison with yielding in t_{rise} = 400 ps compression. The term "broken" here means that the cage changes in a different way to its behavior at t_{rise} = 400 ps, and so it cannot sustain shear stress after yielding. We observe that the fraction of extra cage breakage remains as small as 1% in the rate-insensitive regime [Fig. 6(c)], suggesting that the yielding behavior for these rates is almost the same as that for t_{rise} = 400 ps. Meanwhile, sharp increases in both atom fractions with $d^i_{X,Y} > 1.0$ Å and the distance between yielding replicas, as well as Y/G^y, are observed at $t_{rise} \approx 150$ ps. This suggests that there is an extensive occurrence of extra cage breakage at high strain rates. For instance, Fig. 6(d) shows that the extra broken cages are dispersed throughout the bulk of the yielding replica in the case of t_{rise} = 67 ps. Note that the extra breakages are not related to born defects and will not cooperate. Therefore, the activation volume of extra breakage should be as small as several atoms, which is much smaller than that for the CSM. It is well known that small activation leads to a higher strain-rate-sensitive factor $m = \sqrt{3}k_BT/\sigma V^*$ (where V^* is the activation volume). Thus, our observation provides strong evidence for a transition in the yielding from the activation of born plasticity carriers to a mechanism aided by the nucleation of new carriers.

From the above discussions, our results indicate the surprising extrapolation that there should be minimal variation in excess temperature when the rise time is varied from 10^1 to 10^2 ns in typical QIC experiments. This is due to the fact that both scaled strength and β_{int} are insensitive to strain rate within this range, which may also hold under experimental conditions. To effectively manipulate the thermodynamic path, it is necessary to change the initial temperature of the sample or to manipulate the internal structure to control the yield strength at low strain rates in QIC experiments. Additionally, our data suggest that there may be a significant increase in excess temperature as the rise time is decreased to the nanosecond regime or lower in these experiments.[92]

D. Entropy, configurational entropy, and vibrational entropy

Direct calculation of the thermodynamic entropy increase provides a quantification of dissipation in parallel with the excess temperature. In the NEMD-QIC simulations, we observe that, as well as excess temperature, ΔS at ρ/ρ_0 = 1.29 exhibits a transition from rate-insensitive to rate-sensitive behavior, as depicted in Fig. 7(b). As $t_{rise} > 150$ ps, ΔS remains constant at ~0.6 k_B/atom at ρ/ρ_0 = 1.29, and the production rate is about 2.0×10^{-2} k_B/atom per GPa. However, as t_{rise} decreases to ~30 ps, which is comparable to the adiabatic shock compression wave front width, ΔS at ρ/ρ_0 = 1.29 approaches 0.7 k_B/atom, with a slight increase compared with that for rate-insensitive compression. For comparison, we also calculate ΔS for adiabatic shock compression to ρ/ρ_0 = 1.29, with a value of ~1.6 k_B/atom. This is significantly higher than that for all QICs, in agreement with the thermodynamic theory. This direct quantification of entropy reveals that QIC is substantially different from shock compression, even when the ramp wave width is as small as 30 ps. It should also be stressed that Eq. (2) decomposes the entropy increase into an isothermal compression contribution and an isochoric heating contribution. In the elastic regime, these two contributions cancel each other out, resulting in an isentropic process, as expected. On yielding, the positive isochoric heating contribution becomes dominant over the negative isothermal compression contribution, leading to an overall increase in entropy.
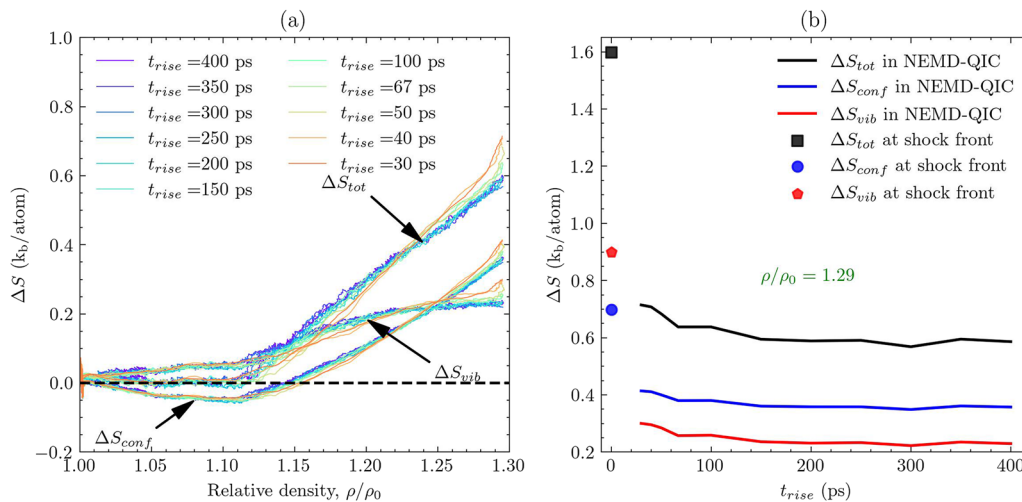

FIG. 7. (a) Total entropy increase ΔS_{tot}, configurational entropy increase ΔS_{conf}, and vibrational entropy increase ΔS_{vib} vs relative density during NEMD-QIC. (b) Entropy increases at ρ/ρ_0 = 1.29 vs rise time. The entropy increases for shock compression (t_{rise} = 0 ps) are also shown.

An advantage of entropy quantification is that it can reveal how the dissipated energy is partitioned. Entropy is split into two parts, a vibrational part S_{vib} and a configurational part S_{conf}, as shown in Fig. 7(a). From the perspective of the potential energy landscape (PEL),[93,94] S_{vib} arises from intrabasin vibration, while S_{conf} arises from interbasin exploration, which is enhanced during plastic deformation. It is important to note that S_{conf} is a thermodynamic measure of structural change, as has been discussed extensively in the literature.[59,63,67,68] We find that the magnitude of ΔS_{conf} in plastically compressed MG subjected to QICs is on the order of 10^{-1} k_B/atom per plastic strain of 0.1 [Fig. 7(a)]. This is comparable to that in the melting of an MG.[73] This fact suggests that MGs also undergo rejuvenation under dynamic compression, even though the increase in density leads to free volume reduction and local order increase in terms of LFFS. Our result implies that the essential structural change in rejuvenation is the diversity of local atomic structures instead of the local symmetry, which will be demonstrated later.

It should be emphasized that the increase in ΔS_{vib} is coupled with ΔS_{conf}. In a highly harmonic approximation, ΔS_{vib} can be estimated as

$$\Delta S_{vib} = 3N \ln \left[\frac{U_K(\rho)}{U_K(\rho_0)} \frac{\overline{\omega(\rho_0)}}{\overline{\omega(\rho)}} \right],$$

where N is the number of atoms, U_K is the kinetic–vibrational energy, and $\overline{\omega}$ is the average vibrational frequency. With little structural change in the elastic regime, the relation $U_K \propto \overline{\omega}$ is established and leads to $\Delta S_{vib} \sim 0$. Figure 7(a) shows that ΔS_{vib} is relatively small in the elastic regime of all QICs. The immediate increase of ΔS_{vib} on yielding is attributed to vibrational mode softening caused by structural change,[95] which is reflected by ΔS_{conf}. As compression proceeds, $U_K \propto \overline{\omega}$ may be reestablished, and saturation of ΔS_{vib} is observed, as in Fig. 7(a). The saturation of ΔS_{vib} in a real QIC is also reasonable, because ΔT_{ise} may totally prevail over ΔT_{excess} at very high density. Additionally, the increase in ΔS_{conf} lags behind that in ΔS_{vib}, but contributes more at $\rho/\rho_0 = 1.29$ to the overall entropy increase in our low-pressure QICs. This is in agreement with the

continuous evolution of the microstructure of MGs under QIC. Therefore, it can be concluded that plastic deformation-induced microstructural change is the fundamental cause of the entropy increase in MGs subjected to QIC in a low-pressure regime.

E. Microstructural change, configurational entropy, and effective temperature

An analysis is performed to investigate the relationship between structural change, thermodynamics, and β_{int}. Microstructural changes in an MG can be described by LFFS and the Shannon entropy S_{Shan} defined on the LFFS distribution.[83,96] As shown in Fig. 8, an increase in LFFS is observed under QIC with increasing density. Note that LFFS of an MG usually decreases under normal plastic deformation without hydrodynamic pressure. This decrease in LFFS can be explained by the more liquid-like structure associated with the continuous rejuvenation and an increase in accessible inherent structures.[85,97] Along the rejuvenation direction toward liquid, the configurational entropy should increase.[73] Figures 7(a) and 8(a) clearly imply the opposite, i.e., that the configurational entropy and LFFS all increase with plastic strain under QIC. These striking results suggest that LFFS may not be able to represent the plasticity carriers in an MG. However, Figs. 7(a) and 8(b) show a continuous decrease in S_{Shan}^{Cu} using only a copper-centered polyhedron, and an increase in S_{conf} as compression proceeds from yielding. This trend was also observed by Han et al.,[83] who quantified configurational entropy from PEL diversity sampling and defined S_{Shan} in the same way as we have done. Thus, the Shannon entropy, which characterizes structural diversity, rather than LFFS, which characterizes the average local structure, is more suitable to describe the microstructural changes during plastic deformation of MGs. We also observe in Fig. 8(b) that at $\rho \approx 1.05\rho_0$, pressure may dominate the structural change, causing an abrupt decrease in S_{Shan}^{Cu}.

It is quite interesting that in the rate-insensitive regime, our S_{conf} and S_{Shan}^{Cu} fall on almost the same line [Fig. 9(a)], suggesting their equivalence in describing the structural change of MG. The configurational entropy clearly has a thermodynamic sense,
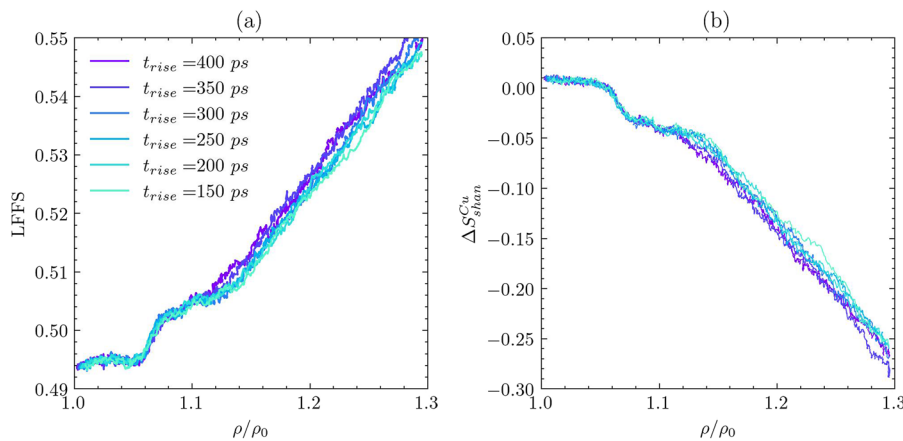

FIG. 8. (a) Local fivefold symmetry (LFFS) vs relative density under compression. (b) Shannon entropy defined on a copper-centered polyhedron distribution vs relative density. Only compressions in the rate-insensitive regime are shown.

while the Shannon entropy is a mathematical description of the microstructure of our atomic model glass. Since the Shannon entropy can be considered in terms of the distribution of local environments of atoms, it is possible to use atomic force microscopy to measure the configurational entropy of an MG. A similar measurable microstructural feature, the fractal dimension of dislocation patterns, is found to increase with plastic deformation.[98] Our work may help relate microstructural characterization with the thermodynamic entropy of the microstructure, thereby providing constraints for plasticity models.[59,99,100]

Another issue of interest is the relation between the configurational entropy and the Taylor–Quinney factor. Figure 9(b) shows that β_{int} increases monotonically with S_{conf} on yielding. This is consistent with Langer's proposal[58–61,63] that β_{int} depends on the interplay between the configurational subsystem and vibrational subsystem. As the compression proceeds after yielding, the configurational entropy increases with plastic strain, suggesting that more and more accessible inherent states and degrees of freedom are activated by deformation. Thus, it is speculated that plastic work becomes more easily converted into heat as the configurational entropy increases. Figure 9(b) also shows that β_{int} vs ΔS_{conf} falls onto almost the same master curve for compressions in the rate-insensitive regime. The following formula, without any physical preconditions, fits this master curve very well:

$$\beta_{int} = 1 - \exp\left[-\left(\frac{\Delta S_{conf} - \Delta S_C}{a}\right)^b\right]. \quad (14)$$

The fitting parameters ΔS_C, a, and b are −0.044, 0.234, and 0.662, respectively. It is interesting that $\exp\left[-\left(\frac{\Delta S_{conf} - \Delta S_C}{a}\right)^b\right](b < 1)$ is of Kohlrausch–Williams–Watts (KWW) form, which is usually used in describing relaxation of glasses.

The effective temperature T_{eff} is defined as the conjugate of the configurational entropy, $T_{eff} \equiv \partial U_C / \partial S_{conf}$,[59,100] where U_C is the configurational energy, or, less accurately, "defect" energy, while, obviously, T is the conjugate of the vibrational entropy,

$T \equiv \partial U_V / \partial S_{vib}$, where U_V is the internal energy minus U_C. We simply calculate U_C as $W_p - Q = (1 - \beta_{int})W_p$. Figure 10(a) shows that U_C increases significantly after yielding and decreases slightly in late compression, while S_{conf} continues increasing. This suggests that the energy storage capability of the configurational subsystem of an MG is limited during QIC compression. Polynomial functions are used to fit the data in Figs. 7(a) and 10(a) (replacing relative density with plastic strain). With these polynomials, the effective temperature is calculated as

$$T_{eff} \equiv \frac{\partial U_C / \partial \varepsilon_p}{\partial S_{conf} / \partial \varepsilon_p}.$$

The trend of decreasing T_{eff} with plastic strain after yielding is depicted in Fig. 10(b). The extremely high T_{eff} on yielding can be considered to be a result of mechanical rejuvenation associated with yielding.[69,70] After yielding, the fact that T_{eff} gradually decreases indicates that the physical aging effect starts to favor mechanical rejuvenation,[24,26] which is expected in plastic deformation of MGs. T_{eff} becomes lower than the thermodynamic temperature at $\varepsilon_p \approx 0.05$ and becomes negative at $\varepsilon_p \approx 0.09$, at which point U_C starts to decrease, suggesting a unique nonequilibrium state. The entropy of the configurational subsystem becomes a nondecreasing function of energy at $\varepsilon_p \approx 0.09$. T_{eff} should have a similar trend to that of T.[59] The higher the value of T_{eff}, the more disordered should the configurational subsystem be. In this sense, the most disordered state is expected to occur at yielding, which causes an extreme mechanical rejuvenation in MGs, and the configurational subsystem evolves toward the direction of order after yielding, while the configurational entropy keeps increasing. Note that Fig. 8(a) indeed indicates that the structure of an MG under QIC evolves toward greater and greater order, characterized by increasing LFFS. This suggests that the heat capacity for the configurational subsystem is first negative and then positive under QIC. Unfortunately, to the best of our knowledge, there is no appropriate theory that can explain our results, even though we have successfully obtained the effective temperature as expected from Ref. 59.
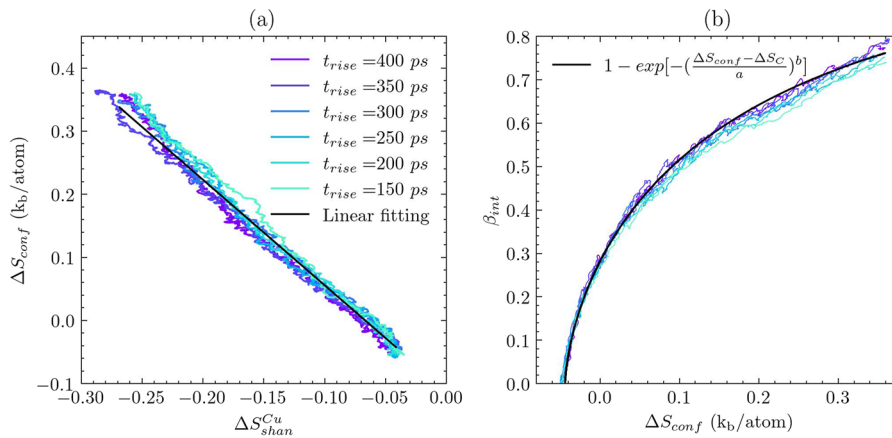

FIG. 9. (a) Configurational entropy vs Shannon entropy defined on copper-centered polyhedron distribution. (b) Taylor–Quinney factor (TQF) vs configurational entropy change during plastic regime for NEMD-QIC. Only compressions in the rate-insensitive regime are shown. Black solid lines are fitting curves.
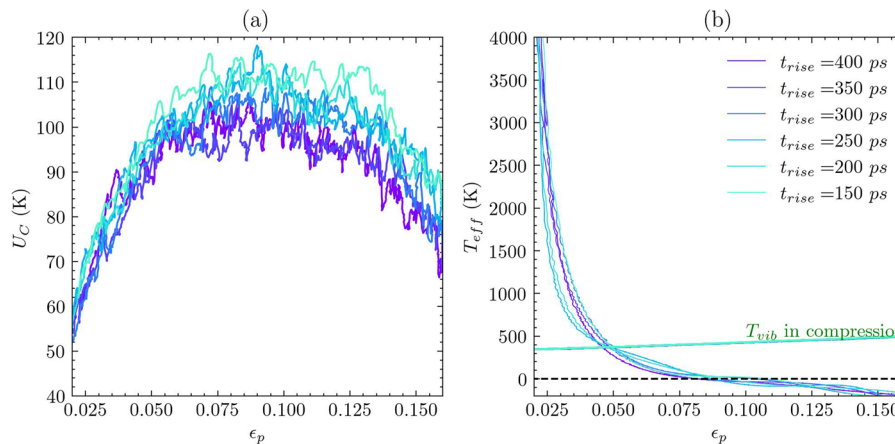
FIG. 10. (a) Configurational energy vs plastic strain. (b) Effective temperature and temperature vs plastic strain. Only compressions in the rate-insensitive regime are shown.

V. CONCLUSION

We have presented a framework for the analysis of the thermodynamic path undergone by a metallic glass subjected to compression and to provide insight into plastic heating. Using this framework, it is possible to accurately recover the same isentrope of the initial sample from P–ρ–T paths obtained by both isotropic compression and NEMD simulations. The deviation from the isentrope is quantified using the excess temperature and thermodynamic entropy. We have demonstrated that this deviation stems from plasticity under QIC of metallic glass and quantifies the portion of plastic work being dissipated. Our results suggest that rate-insensitive entropy production under compression with strain rates achievable experimentally is of the order of $10^{-2} k_B$/atom per GPa. However, at higher strain rates, a transition from rate-insensitive to rate-sensitive entropy production is observed, which is attributed to the breakdown of the relation $Y/G^\gamma \approx$ const. In particular, the entropy is partitioned into configurational and vibrational entropies. Thus, the framework can provide a thermodynamic variable to describe microstructural change. The configurational entropy is found to be proportional to the Shannon entropy form describing structural change. Overall, our framework provides a comprehensive understanding of compression, plastic deformation, structural change, entropy production, and their relationships in QIC. Furthermore, it greatly extends the capability of atomistic simulations to interpret QIC experiments.

SUPPLEMENTARY MATERIAL

See the supplementary material for details of sample reparation, NEMD simulation methods, strain decomposition, free energy calculation, microstructure characterization, and size/strain rate effect check.

AUTHOR DECLARATIONS

Conflict of Interest

The authors have no conflicts to disclose.

Author Contributions

Kaiguo Chen: Conceptualization (equal); Data curation (equal); Formal analysis (equal); Investigation (equal); Methodology (equal); Writing – original draft (equal); Writing – review & editing (equal). **Bo Chen**: Formal analysis (equal); Methodology (equal); Writing – original draft (equal). **Yinan Cui**: Data curation (equal); Formal analysis (equal); Writing – review & editing (equal). **Yuying Yu**: Investigation (equal); Supervision (equal); Writing – original draft (equal). **Jidong Yu**: Investigation (equal); Software (equal); Validation (equal). **Huayun Geng**: Supervision (equal); Validation (equal). **Dongdong Kang**: Methodology (equal); Project administration (equal). **Jianhua Wu**: Investigation (equal); Resources (equal). **Yao Shen**: Formal analysis (equal); Project administration (equal); Supervision (equal); Writing – original draft (equal); Writing – review & editing (equal). **Jiayu Dai**: Methodology (equal); Project administration (equal); Resources (equal); Supervision (equal); Writing – original draft (equal); Writing – review & editing (equal).

DATA AVAILABILITY

The data that support the findings of this study are available on request from the corresponding author.

REFERENCES

[1]H.-K. Mao, B. Chen, J. Chen, K. Li, J.-F. Lin, W. Yang, and H. Zheng, "Recent advances in high-pressure science and technology," Matter Radiat. Extremes **1**(1), 59–75 (2016).

[2]R. Betti and O. A. Hurricane, "Inertial-confinement fusion with lasers," Nat. Phys. **12**(5), 435–448 (2016).

[3]S. Nakai and H. Takabe, "Principles of inertial confinement fusion–physics of implosion and the concept of inertial fusion energy," Rep. Prog. Phys. **59**(9), 1071 (1996).

[4]V. N. Goncharov, O. V. Gotchev, E. Vianello, T. R. Boehly, J. P. Knauer, P. W. McKenty, P. B. Radha, S. P. Regan, T. C. Sangster, S. Skupsky, V. A. Smalyuk, R. Betti, R. L. McCrory, D. D. Meyerhofer, and C. Cherfils-Clérouin, "Early stage of implosion in inertial confinement fusion: Shock timing and perturbation evolution," Phys. Plasmas **13**(1), 012702 (2006).

[5]R. S. Craxton, K. S. Anderson, T. R. Boehly, V. N. Goncharov, D. R. Harding, J. P. Knauer, R. L. McCrory, P. W. McKenty, D. D. Meyerhofer, J. F. Myatt, A. J. Schmitt, J. D. Sethian, R. W. Short, S. Skupsky, W. Theobald, W. L. Kruer, K. Tanaka, R. Betti, T. J. B. Collins, J. A. Delettrez, S. X. Hu, J. A. Marozas, A. V. Maximov, D. T. Michel, P. B. Radha, S. P. Regan, T. C. Sangster, W. Seka, A. A. Solodov, J. M. Soures, C. Stoeckl, and J. D. Zuegel, "Direct-drive inertial confinement fusion: A review," Phys. Plasmas **22**(11), 110501 (2015).

[6]D. Kang, Y. Hou, Q. Zeng, and J. Dai, "Unified first-principles equations of state of deuterium-tritium mixtures in the global inertial confinement fusion region," Matter Radiat. Extremes **5**(5), 055401 (2020).

[7]J. Lütgert, M. Bethkenhagen, B. Bachmann, L. Divol, D. O. Gericke, S. H. Glenzer, G. N. Hall, N. Izumi, S. F. Khan, O. L. Landen, S. A. MacLaren, L. Masse, R. Redmer, M. Schörner, M. O. Schölmerich, S. Schumacher, N. R. Shaffer, C. E. Starrett, P. A. Sterne, C. Trosseille, T. Döppner, and D. Kraus, "Platform for probing radiation transport properties of hydrogen at conditions found in the deep interiors of red dwarfs," Phys. Plasmas **29**(8), 083301 (2022).

[8]B. Remington, "Exploring the universe through Discovery Science on the NIF," in *2021 IEEE International Conference on Plasma Science (ICOPS), Lake Tahoe, NV, 12-16 September 2021* (IEEE, 2021).

[9]B. Remington, "Dynamic materials experiments at ultrahigh pressures and strain rates on the National Ignition Facility laser," AGU Fall Meeting 2021, New Orleans, LA, 13-17 December 2021, paper DI35C-0042 (2021).

[10]A. Krygier, P. D. Powell, J. M. McNaney, C. M. Huntington, S. T. Prisbrey, B. A. Remington, R. E. Rudd, D. C. Swift, C. E. Wehrenberg, A. Arsenlis, H. S. Park, P. Graham, E. Gumbrell, M. P. Hill, A. J. Comley, and S. D. Rothman, "Extreme hardening of Pb at high pressure and strain rate," Phys. Rev. Lett. **123**(20), 205701 (2019).

[11]N. Jourdain, U. Chaulagain, M. Havlík, D. Kramer, D. Kumar, I. Majerová, V. T. Tikhonchuk, G. Korn, and S. Weber, "The L4n laser beamline of the P3-installation: Towards high-repetition rate high-energy density physics at ELI-beamlines," Matter Radiat. Extremes **6**(1), 015401 (2020).

[12]D. Riley, *Shock and Ramp Compression, Warm Dense Matter* (IOP Publishing, 2021).

[13]S. C. Grant, T. Ao, C. T. Seagle, A. J. Porwitzky, J.-P. Davis, K. R. Cochrane, D. H. Dolan, J.-F. Lin, T. Ditmire, and A. C. Bernstein, "Equation of state measurements on iron near the melting curve at planetary core conditions by shock and ramp compressions," J. Geophys. Res.: Solid Earth **126**(3), e2020JB020008, https://doi.org/10.1029/2020jb020008 (2021).

[14]G.-J. Li, Z.-G. Li, Q.-F. Chen, Y.-J. Gu, W. Zhang, L. Liu, H.-Y. Geng, Z.-Q. Wang, Y.-S. Lan, Y. Hou, J.-Y. Dai, and X.-R. Chen, "Multishock to quasi-isentropic compression of dense gaseous deuterium-helium mixtures up to 120 GPa: Probing the sound velocities relevant to planetary interiors," Phys. Rev. Lett. **126**(7), 075701 (2021).

[15]S. Saeki, "Empirical determination of the three-dimensional isentropic equation of state of polyethylene," High Pressure Res. **40**(2), 219–234 (2020).

[16]K. Miyanishi, N. Ozaki, E. Brambrink, H. G. Wei, A. Benuzzi-Mounaix, A. Ravasio, A. Diziere, T. Vinci, M. Koenig, and R. Kodama, "EOS measurements of pressure standard materials using laser-driven ramp-wave compression technique," J. Phys.: Conf. Ser. **215**, 012199 (2010).

[17]H. Park, B. A. Remington, D. Braun, P. Celliers, G. W. Collins, J. Eggert, E. Giraldez, S. L. Pape, T. Lorenz, B. Maddox, A. Hamza, D. Ho, D. Hicks, P. Patel, S. Pollaine, S. Prisbrey, R. Smith, D. Swift, and R. Wallace, "Quasi-isentropic material property studies at extreme pressures: From omega to NIF," J. Phys.: Conf. Ser. **112**(4), 042024 (2008).

[18]J. L. Ding and J. R. Asay, "Material characterization with ramp wave experiments," J. Appl. Phys. **101**(7), 073517 (2007).

[19]V. Fortov, *Shock Compression Thermodynamics, Intense Shock Waves on Earth and in Space* (Springer International Publishing, Cham, 2021), pp. 19–31.

[20]C. E. Wehrenberg, D. McGonegle, C. Bolme, A. Higginbotham, A. Lazicki, H. J. Lee, B. Nagler, H. S. Park, B. A. Remington, R. E. Rudd, M. Sliwa, M. Suggit, D. Swift, F. Tavella, L. Zepeda-Ruiz, and J. S. Wark, "*In situ* X-ray diffraction measurement of shock-wave-driven twinning and lattice dynamics," Nature **550**(7677), 496–499 (2017).

[21]E. M. Bringa, K. Rosolankova, R. E. Rudd, B. A. Remington, J. S. Wark, M. Duchaineau, D. H. Kalantar, J. Hawreliak, and J. Belak, "Shock deformation of face-centred-cubic metals on subnanosecond timescales," Nat. Mater. **5**(10), 805–809 (2006).

[22]F. González-Cataldo, B. K. Godwal, K. Driver, R. Jeanloz, and B. Militzer, "Model of ramp compression of diamond from *ab initio* simulations," Phys. Rev. B **104**(13), 134104 (2021).

[23]J. R. Macdonald, "Review of some experimental and analytical equations of state," Rev. Mod. Phys. **41**(2), 316–349 (1969).

[24]A. Higginbotham, J. Hawreliak, E. M. Bringa, G. Kimminau, N. Park, E. Reed, B. A. Remington, and J. S. Wark, "Molecular dynamics simulations of ramp-compressed copper," Phys. Rev. B **85**(2), 024112 (2012).

[25]W. Li, E. N. Hahn, P. S. Branicio, X. Yao, X. Zhang, B. Feng, and T. C. Germann, "Rate dependence and anisotropy of SiC response to ramp and wave-free quasi-isentropic compression," Int. J. Plast. **138**, 102923 (2021).

[26]Y. Ping, F. Coppari, D. G. Hicks, B. Yaakobi, D. E. Fratanduono, S. Hamel, J. H. Eggert, J. R. Rygg, R. F. Smith, D. C. Swift, D. G. Braun, T. R. Boehly, and G. W. Collins, "Solid iron compressed up to 560 GPa," Phys. Rev. Lett. **111**(6), 065501 (2013).

[27]A. Lazicki, D. McGonegle, J. R. Rygg, D. G. Braun, D. C. Swift, M. G. Gorman, R. F. Smith, P. G. Heighway, A. Higginbotham, M. J. Suggit, D. E. Fratanduono, F. Coppari, C. E. Wehrenberg, R. G. Kraus, D. Erskine, J. V. Bernier, J. M. McNaney, R. E. Rudd, G. W. Collins, J. H. Eggert, and J. S. Wark, "Metastability of diamond ramp-compressed to 2 terapascals," Nature **589**(7843), 532–535 (2021).

[28]R. F. Smith, J. H. Eggert, R. Jeanloz, T. S. Duffy, D. G. Braun, J. R. Patterson, R. E. Rudd, J. Biener, A. E. Lazicki, A. V. Hamza, J. Wang, T. Braun, L. X. Benedict, P. M. Celliers, and G. W. Collins, "Ramp compression of diamond to five terapascals," Nature **511**(7509), 330–333 (2014).

[29]D. E. Fratanduono, R. F. Smith, S. J. Ali, D. G. Braun, A. Fernandez-Pañella, S. Zhang, R. G. Kraus, F. Coppari, J. M. McNaney, M. C. Marshall, L. E. Kirch, D. C. Swift, M. Millot, J. K. Wicks, and J. H. Eggert, "Probing the solid phase of noble metal copper at terapascal conditions," Phys. Rev. Lett. **124**(1), 015701 (2020).

[30]D. K. Bradley, J. H. Eggert, R. F. Smith, S. T. Prisbrey, D. G. Hicks, D. G. Braun, J. Biener, A. V. Hamza, R. E. Rudd, and G. W. Collins, "Diamond at 800 GPa," Phys. Rev. Lett. **102**(7), 075503 (2009).

[31]J. L. Ding and J. R. Asay, "Numerical study of rate-dependent strength behavior under ramp and shock wave loading," Int. J. Plast. **25**(4), 695–714 (2009).

[32]J. L. Ding, "Thermal and mechanical analysis of material response to non-steady ramp and steady shock wave loading," J. Mech. Phys. Solids **54**(2), 237–265 (2006).

[33]Z. Xie, W.-R. Jian, S. Xu, I. J. Beyerlein, X. Zhang, X. Yao, and R. Zhang, "Phase transition in medium entropy alloy CoCrNi under quasi-isentropic compression," Int. J. Plast. **157**, 103389 (2022).

[34]K. Ren, H. Liu, R. Ma, S. Chen, S. Zhang, R. Wang, R. Chen, Y. Tang, S. Li, and F. Lu, "Dynamic compression behavior of TiZrNbV refractory high-entropy

alloys upon ultrahigh strain rate loading," J. Mater. Sci. Technol. **161**, 201–219 (2023).

[35] D. N. Blaschke, A. Hunter, and D. L. Preston, "Analytic model of the remobilization of pinned glide dislocations: Including dislocation drag from phonon wind," Int. J. Plast. **131**, 102750 (2020).

[36] M. W. Guinan and D. J. Steinberg, "Pressure and temperature derivatives of the isotropic polycrystalline shear modulus for 65 elements," J. Phys. Chem. Solids **35**(11), 1501–1512 (1974).

[37] K. V. Khishchenko and A. E. Mayer, "High- and low-entropy layers in solids behind shock and ramp compression waves," Int. J. Mech. Sci. **189**, 105971 (2021).

[38] M. Sliwa, D. McGonegle, C. Wehrenberg, C. A. Bolme, P. G. Heighway, A. Higginbotham, A. Lazicki, H. J. Lee, B. Nagler, H. S. Park, R. E. Rudd, M. J. Suggit, D. Swift, F. Tavella, L. Zepeda-Ruiz, B. A. Remington, and J. S. Wark, "Femtosecond X-ray diffraction studies of the reversal of the microstructural effects of plastic deformation during shock release of tantalum," Phys. Rev. Lett. **120**(26), 265502 (2018).

[39] D. Milathianaki, S. Boutet, G. J. Williams, A. Higginbotham, D. Ratner, A. E. Gleason, M. Messerschmidt, M. M. Seibert, D. C. Swift, P. Hering, J. Robinson, W. E. White, and J. S. Wark, "Femtosecond visualization of lattice dynamics in shock-compressed matter," Science **342**(6155), 220–223 (2013).

[40] R. F. Smith, J. H. Eggert, A. Jankowski, P. M. Celliers, M. J. Edwards, Y. M. Gupta, J. R. Asay, and G. W. Collins, "Stiff response of aluminum under ultrafast shockless compression to 110 GPA," Phys. Rev. Lett. **98**(6), 065701 (2007).

[41] D. N. Polsin, D. E. Fratanduono, J. R. Rygg, A. Lazicki, R. F. Smith, J. H. Eggert, M. C. Gregor, B. J. Henderson, X. Gong, J. A. Delettrez, R. G. Kraus, P. M. Celliers, F. Coppari, D. C. Swift, C. A. McCoy, C. T. Seagle, J.-P. Davis, S. J. Burns, G. W. Collins, and T. R. Boehly, "X-ray diffraction of ramp-compressed aluminum to 475 GPa," Phys. Plasmas **25**(8), 082709 (2018).

[42] D. N. Polsin, A. Lazicki, X. Gong, S. J. Burns, F. Coppari, L. E. Hansen, B. J. Henderson, M. F. Huff, M. I. McMahon, M. Millot, R. Paul, R. F. Smith, J. H. Eggert, G. W. Collins, and J. R. Rygg, "Structural complexity in ramp-compressed sodium to 480 GPa," Nat. Commun. **13**(1), 2534 (2022).

[43] R. F. Smith, J. H. Eggert, R. E. Rudd, D. C. Swift, C. A. Bolme, and G. W. Collins, "High strain-rate plastic flow in Al and Fe," J. Appl. Phys. **110**(12), 123515 (2011).

[44] D. C. Wallace, "Irreversible thermodynamics of overdriven shocks in solids," Phys. Rev. B **24**(10), 5597–5606 (1981).

[45] K. Yang, Y. Wu, Y. Wu, F. Huang, T. Chong, Z. Zhang, and X. Zheng, "A unified model of anisotropy, thermoelasticity, inelasticity, phase transition and reaction for high-pressure ramp-loaded RDX single crystal," Int. J. Plast. **144**, 103048 (2021).

[46] G. I. Taylor and H. Quinney, "The latent energy remaining in a metal after cold working," Proc. R. Soc. London, Ser. A **143**(849), 307–326 (1934).

[47] D. J. Luscher, M. A. Buechler, D. J. Walters, C. A. Bolme, and K. J. Ramos, "On computing the evolution of temperature for materials under dynamic loading," Int. J. Plast. **111**, 188–210 (2018).

[48] D. J. Luscher, J. R. Mayeur, H. M. Mourad, A. Hunter, and M. A. Kenamond, "Coupling continuum dislocation transport with crystal plasticity for application to shock loading conditions," Int. J. Plast. **76**, 111–129 (2016).

[49] Y. Cui, T. Wang, S. Luo, Z. Li, and Z. Li, "A discrete–continuous model of three-dimensional dislocation elastodynamics," Int. J. Plast. **152**, 103221 (2022).

[50] J. J. Mason, A. J. Rosakis, and G. Ravichandran, "On the strain and strain rate dependence of the fraction of plastic work converted to heat: An experimental study using high speed infrared detectors and the Kolsky bar," Mech. Mater **17**(2), 135–145 (1994).

[51] D. Rittel, L. H. Zhang, and S. Osovski, "The dependence of the Taylor–Quinney coefficient on the dynamic loading mode," J. Mech. Phys. Solids **107**, 96–114 (2017).

[52] J. C. Nieto-Fuentes, D. Rittel, and S. Osovski, "On a dislocation-based constitutive model and dynamic thermomechanical considerations," Int. J. Plast. **108**, 55–69 (2018).

[53] J. C. Nieto-Fuentes, S. Osovski, A. Venkert, and D. Rittel, "Reassessment of the dynamic thermomechanical conversion in metals," Phys. Rev. Lett. **123**(25), 255502 (2019).

[54] A. Zubelewicz, "Century-long Taylor-Quinney interpretation of plasticity-induced heating reexamined," Sci. Rep. **9**(1), 9088 (2019).

[55] N. C. Ferreri, Z. Feng, D. J. Savage, D. W. Brown, B. Clausen, T. A. Sisneros, and M. Knezevic, "In-situ high-energy X-ray diffraction and crystal plasticity modeling to predict the evolution of texture, twinning, lattice strains and strength during loading and reloading of beryllium," Int. J. Plast. **150**, 103217 (2022).

[56] Q.-l. Xiong, Z. Li, T. Shimada, and T. Kitamura, "Atomistic investigation on the conversion of plastic work to heat in high-rate shear deformation," Int. J. Plast. **149**, 103158 (2022).

[57] J. C. Stimac, N. Bertin, J. K. Mason, and V. V. Bulatov, "Energy storage under high-rate compression of single crystal tantalum," Acta Mater. **239**, 118253 (2022).

[58] J. S. Langer, "Statistical thermodynamics of crystal plasticity," J. Stat. Phys **175**(3), 531–541 (2019).

[59] E. Bouchbinder and J. S. Langer, "Nonequilibrium thermodynamics of driven amorphous materials. II. Effective-temperature theory," Phys. Rev. E **80**(3), 031132 (2009).

[60] K. C. Le, T. M. Tran, and J. S. Langer, "Thermodynamic dislocation theory of high-temperature deformation in aluminum and steel," Phys. Rev. E **96**(1), 013004 (2017).

[61] J. S. Langer, E. Bouchbinder, and T. Lookman, "Thermodynamic theory of dislocation-mediated plasticity," Acta Mater. **58**(10), 3718–3732 (2010).

[62] K. C. Le, "Two universal laws for plastic flows and the consistent thermodynamic dislocation theory," Mech. Res. Commun. **109**, 103597 (2020).

[63] J. S. Langer and K. C. Le, "Scaling confirmation of the thermodynamic dislocation theory," Proc. Natl. Acad. Sci. U. S. A. **117**(47), 29431–29434 (2020).

[64] S. Roy Chowdhury and D. Roy, "A non-equilibrium thermodynamic model for viscoplasticity and damage: Two temperatures and a generalized fluctuation relation," Int. J. Plast. **113**, 158–184 (2019).

[65] S.-C. Dai, Z.-C. Xie, and Y.-J. Wang, "Atomistic interpretation of extra temperature and strain-rate sensitivity of heterogeneous dislocation nucleation in a multi-principal-element alloy," Int. J. Plast. **149**, 103155 (2022).

[66] V. L. Berdichevsky, "Entropy of microstructure," J. Mech. Phys. Solids **56**(3), 742–771 (2008).

[67] V. L. Berdichevsky, "Thermodynamics of microstructure evolution: Grain growth," Int. J. Eng. Sci. **57**, 50–78 (2012).

[68] V. L. Berdichevsky, "Beyond classical thermodynamics: Dislocation-mediated plasticity," J. Mech. Phys. Solids **129**, 83–118 (2019).

[69] W. Rao, Y. Chen, and L.-H. Dai, "A constitutive model for metallic glasses based on two-temperature nonequilibrium thermodynamics," Int. J. Plast. **154**, 103309 (2022).

[70] R. Xiao, C. Tian, Y. Xu, and P. Steinmann, "Thermomechanical coupling in glassy polymers: An effective temperature theory," Int. J. Plast. **156**, 103361 (2022).

[71] S. Ogata, F. Shimizu, J. Li, M. Wakeda, and Y. Shibutani, "Atomistic simulation of shear localization in Cu–Zr bulk metallic glass," Intermetallics **14**(8), 1033–1037 (2006).

[72] Y. Wang, Y. Wang, and J. Zhang, "Connecting shear localization with the long-range correlated polarized stress fields in granular materials," Nat. Commun. **11**(1), 4349 (2020).

[73] R. Alvarez-Donado and A. Antonelli, "Splitting up entropy into vibrational and configurational contributions in bulk metallic glasses: A thermodynamic approach," Phys. Rev. Res. **2**(1), 013202 (2020).

[74] Y. Q. Cheng, E. Ma, and H. W. Sheng, "Atomic level structure in multicomponent bulk metallic glass," Phys. Rev. Lett. **102**(24), 245501 (2009).

[75] S. Plimpton, "Fast parallel algorithms for short-range molecular dynamics," J. Comput. Phys. **117**(1), 1–19 (1995).

[76] A. P. Thompson, H. M. Aktulga, R. Berger, D. S. Bolintineanu, W. M. Brown, P. S. Crozier, P. J. in't Veld, A. Kohlmeyer, S. G. Moore, T. D. Nguyen, R. Shan, M. J. Stevens, J. Tranchida, C. Trott, and S. J. Plimpton, "LAMMPS—A flexible simulation tool for particle-based materials modeling at the atomic, meso, and continuum scales," Comput. Phys. Commun. **271**, 108171 (2022).

[77] A. E. Mattsson and W. J. Rider, "Artificial viscosity: Back to the basics," Int. J. Numer. Methods Fluids **77**(7), 400–417 (2015).

[78] D. Poulikakos and S. Maruyama, Microscale Thermophys. Eng. **7**(3), 181–206 (2003).

[79] Y. Zhou, Z.-Y. Dong, W.-P. Hsieh, A. F. Goncharov, and X.-J. Chen, "Thermal conductivity of materials under pressure," Nat. Rev. Phys. **4**(5), 319–335 (2022).

[80] B. Shi, S. Yang, S. Liu, and P. Jin, "Lindemann-like rule between average thermal expansion coefficient and glass transition temperature for metallic glasses," J. Non-Cryst. Solids **503–504**, 194–196 (2019).

[81] H. W. Sheng, W. K. Luo, F. M. Alamgir, J. M. Bai, and E. Ma, "Atomic packing and short-to-medium-range order in metallic glasses," Nature **439**(7075), 419–425 (2006).

[82] H. L. Peng, M. Z. Li, and W. H. Wang, "Structural signature of plastic deformation in metallic glasses," Phys. Rev. Lett. **106**(13), 135503 (2011).

[83] D. Han, D. Wei, P.-H. Cao, Y.-J. Wang, and L.-H. Dai, "Statistical complexity of potential energy landscape as a dynamic signature of the glass transition," Phys. Rev. B **101**(6), 064205 (2020).

[84] P. G. Heighway, M. Sliwa, D. McGonegle, C. Wehrenberg, C. A. Bolme, J. Eggert, A. Higginbotham, A. Lazicki, H. J. Lee, B. Nagler, H. S. Park, R. E. Rudd, R. F. Smith, M. J. Suggit, D. Swift, F. Tavella, B. A. Remington, and J. S. Wark, "Nonisentropic release of a shocked solid," Phys. Rev. Lett. **123**(24), 245501 (2019).

[85] F. Shimizu, S. Ogata, and J. Li, "Theory of shear banding in metallic glasses and molecular dynamics calculations," Mater. Trans. **48**(11), 2923–2927 (2007).

[86] A. Stukowski, "Visualization and analysis of atomistic simulation data with OVITO–the Open Visualization Tool," Modell. Simul. Mater. Sci. Eng. **18**(1), 015012 (2010).

[87] D. Frenkel and A. J. C. Ladd, "New Monte Carlo method to compute the free energy of arbitrary solids. Application to the fcc and hcp phases of hard spheres," J. Chem. Phys. **81**(7), 3188–3193 (1984).

[88] X. Y. Li, H. P. Zhang, S. Lan, D. L. Abernathy, T. Otomo, F. W. Wang, Y. Ren, M. Z. Li, and X. L. Wang, "Observation of high-frequency transverse phonons in metallic glasses," Phys. Rev. Lett. **124**(22), 225902 (2020).

[89] W. L. Johnson and K. Samwer, "A universal criterion for plastic yielding of metallic glasses with a $(T/T_g)^{2/3}$ temperature dependence," Phys. Rev. Lett. **95**(19), 195501 (2005).

[90] B. Luo, G. Wang, F. Tan, J. Zhao, C. Liu, and C. Sun, "Dynamic behaviors of a Zr-based bulk metallic glass under ramp wave and shock wave loading," AIP Adv. **5**(6), 067161 (2015).

[91] T. J. Vogler, "On measuring the strength of metals at ultrahigh strain rates," J. Appl. Phys. **106**(5), 053530 (2009).

[92] B. Gurrutxaga-Lerma, D. S. Balint, D. Dini, D. E. Eakins, and A. P. Sutton, "Attenuation of the dynamic yield point of shocked aluminum using elastodynamic simulations of dislocation dynamics," Phys. Rev. Lett. **114**(17), 174301 (2015).

[93] F. H. Stillinger, "A topographic view of supercooled liquids and glass formation," Science **267**(5206), 1935–1939 (1995).

[94] F. H. Stillinger and P. G. Debenedetti, "Energy landscape diversity and supercooled liquid properties," J. Chem. Phys. **116**(8), 3353–3361 (2002).

[95] R. Mahjoub, N. E. Hamilton, K. J. Laws, and M. Ferry, "Softening of phonon spectra in metallic glasses," npj Comput. Mater. **2**(1), 16029 (2016).

[96] D. Han, D. Wei, J. Yang, H.-L. Li, M.-Q. Jiang, Y.-J. Wang, L.-H. Dai, and A. Zaccone, "Atomistic structural mechanism for the glass transition: Entropic contribution," Phys. Rev. B **101**(1), 014113 (2020).

[97] G. Ding, C. Li, A. Zaccone, W. H. Wang, H. C. Lei, F. Jiang, Z. Ling, and M. Q. Jiang, "Ultrafast extreme rejuvenation of metallic glasses by shock compression," Sci. Adv. **5**(8), eaaw6249 (2019).

[98] P. Hähner, K. Bay, and M. Zaiser, "Fractal dislocation patterning during plastic deformation," Phys. Rev. Lett. **81**(12), 2470–2473 (1998).

[99] A. Vinogradov, I. S. Yasnikov, and Y. Estrin, "Evolution of fractal structures in dislocation ensembles during plastic deformation," Phys. Rev. Lett. **108**(20), 205504 (2012).

[100] E. Bouchbinder and J. S. Langer, "Nonequilibrium thermodynamics of driven amorphous materials. I. Internal degrees of freedom and volume deformation," Phys. Rev. E **80**(3), 031131 (2009).